Optics Letters

Super-resolution in diffractive imaging from hemispherical elastic light scattering data

Sergiy Lysenko,[1,*] Valeriy Sterligov,[2] Manuel Gonçalves,[3] Armando Rúa,[1] Iaroslav Gritsayenko,[2] and Félix Fernández[1]

[1]Department of Physics, University of Puerto Rico, Mayaguez, San Juan 00681 Puerto Rico
[2]V. Lashkaryov Institute of Semiconductor Physics, National Academy of Sciences of Ukraine, 41 Nauki Prosp., 03028 Kiev, Ukraine
[3]Ulm University, Institute of Experimental Physics, Albert-Einstein-Allee 11, 89081 Ulm, Germany
*Corresponding author: sergiy.lysenko@upr.edu

Received 28 March 2017; accepted 9 May 2017; posted 16 May 2017 (Doc. ID 291443); published 6 June 2017

Angle-resolved hemispherical elastic light scattering techniques have been used to reconstruct the surface profile of two-dimensional photonic crystals with submicron resolution and metrological precision. Iterative algorithms permit subsequent calculation of a surface autocorrelation function with additional numerical approximation of the power spectrum and then yield final reconstruction of the surface shape. The proposed method enables filtering out unwanted scattering background, precluding the convergence of phase-retrieval algorithms. The estimation of higher harmonics in the power spectrum provides the reconstruction of a realistic surface achieving subwavelength resolution.

OCIS codes: (290.3200) Inverse scattering; (100.3010) Image reconstruction techniques; (100.6640) Superresolution; (290.5880) Scattering, rough surfaces.

https://doi.org/10.1364/OL.42.002263

Space distribution of scattered light contains important information about the illuminated object [1]. Holographic registration enables rigorous reconstruction of the surface relief and spatial distribution of optical inhomogeneities [2]. However, this method requires specific measurement conditions. Also, traditional holography techniques are difficult to apply for monitoring of ultrafast processes in materials or for other *in situ* control of nonstationary optical processes. A single-shot Fourier transform light scattering [3] can improve holographic techniques. In diffractive imaging studies it is much simpler to measure only the intensity of scattered light. However, the phase information in these measurements is lost because of the use of quadratic optoelectronic detectors. As a result, direct reconstruction of surface relief becomes questionable, since it requires information about the amplitude and phase of scattered light.

If the object size is comparable or less than the light wavelength, the phase reconstruction becomes a challenge [4]. Moreover, the object of interest is superimposed often onto a statistically random surface relief, which produces an unwanted scattering background. As a result, the relative contribution of the object into the total scattering field can be small. This makes rigorous reconstruction of the surface

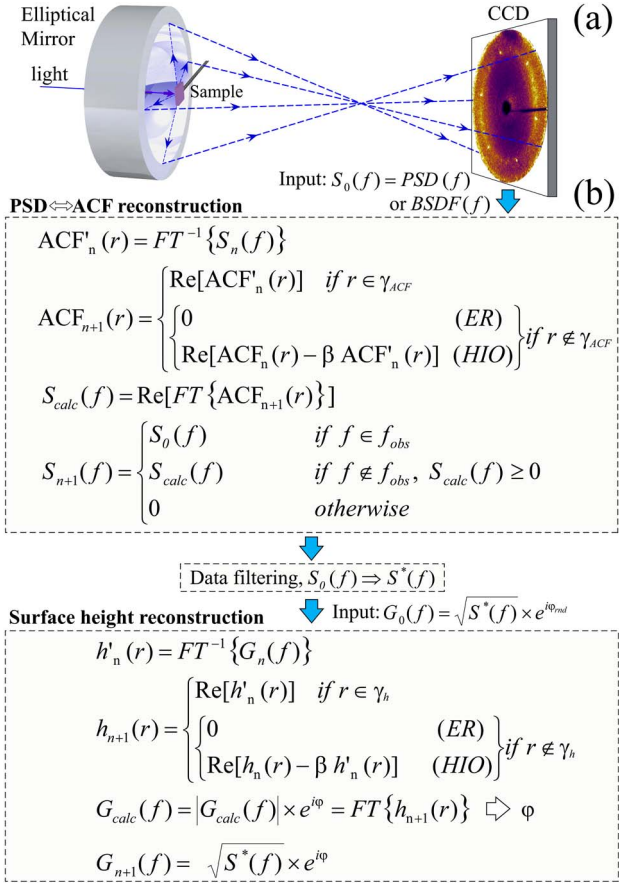

Fig. 1. (a) Schematic layout of the optical setup. (b) The computation algorithm, with three main steps: (1) calculation of ACF with partial reconstruction of power spectral density function $S(f)$; (2) filtering of experimental data (see text for details); and (3) reconstruction of surface profile h. Index n corresponds to the number of iteration. FT and FT^{-1} denote direct and inverse Fourier transform, respectively.

profile impossible by phase-retrieval techniques. Nevertheless, single or periodical objects with a size larger than the light wavelength can be well reconstructed from a scattering indicatrix recorded by conventional CCD or CMOS detectors, applying generalized Gerchberg–Saxton error-reduction (ER) or hybrid input-output (HIO) phase-retrieval algorithms [4–6].

In this Letter, we present a new technique of surface shape reconstruction from angle-resolved hemispherical elastic light scattering (ARHELS) data. Iterative algorithms are applied to reconstruct the phase of scattered field and surface profile with submicron resolution by filtering the diffuse scattering and scattering caused by stochastic relief. Moreover, in this study we extend the ARHELS technique to obtain metrological characteristics of the objects smaller than the light wavelength, achieving super-resolution by reconstructing higher harmonics of the surface power spectral density (PSD) function.

Two-dimensional photonic (PC1) and plasmonic (PC2) crystals were used as test objects. Sample PC1 was grown by self-assembling of polystyrene spheres with an average diameter of 450 nm [7]. Sample PC2 was prepared by shadow nanosphere lithography of gold nanopyramids using 1 μm polystyrene spheres [8].

The ARHELS measurements were performed with an experimental setup [9,10] schematically shown in Fig. 1(a). The incident laser beam (with Gaussian profile) was tightly focused on the sample surface at normal incidence. The 200-mm-diameter elliptical mirror collected scattered light within the hemisphere and projected it on the CCD. The angle-resolved scatter was measured as a function of polar and azimuthal angles, and recalculated to bidirectional-scatter-distribution-function BSDF (f) versus spatial frequency f of surface relief decomposition [1].

BSDF has a close resemblance to PSD of the surface and, therefore, BSDF in most cases can be used for surface analysis instead of the exact PSD function [1]. Thus, either BSDF or PSD can be used for calculation of the autocorrelation function (ACF) and for reconstruction of surface profile $h(r)$, a function of displacement vector r, using ER and HIO algorithms. Figure 1(b) shows the corresponding computational procedures.

The algorithm to compute ACF(r) uses the surface power spectral density function S_0 obtained from ARHELS measurements: $S_0(f) = \mathrm{PSD}(f)$ or $S_0(f) \simeq \mathrm{BSDF}(f)$. The inverse Fourier transform of $S_n(f)$ in the nth iteration is applied to calculate a trial autocorrelation function $\mathrm{ACF}'_n(r)$. We note that the $S(f)$ and ACF(r) functions are real, and $S(f)$ is non-negative. These constraints were applied to obtain $\mathrm{ACF}_{n+1}(r)$ in the successive $n+1$ ER or HIO iteration. γ_{ACF} in Fig. 1(b) is the area where the ACF(r) is nonzero for the ER procedure [11]. Constant β in the HIO algorithm is a feedback parameter. Its value can be chosen arbitrarily between 0.5 and 1.0 [12]. Within some areas the experimental data for the input function $S_0(f)$ is not available. Nevertheless, these data were iteratively reconstructed for the spectrum $S_{n+1}(f)$ by using the Fourier transform of $\mathrm{ACF}_{n+1}(r)$.

To perform the surface height reconstruction, we use the spectrum of surface roughness $G_0(f) = \sqrt{S^*(f)} \times e^{i\varphi_{rnd}}$ as the input function [Fig. 1(b)]. Here $S^*(f)$ is the filtered function of surface power spectral density, and φ_{rnd} is an arbitrary

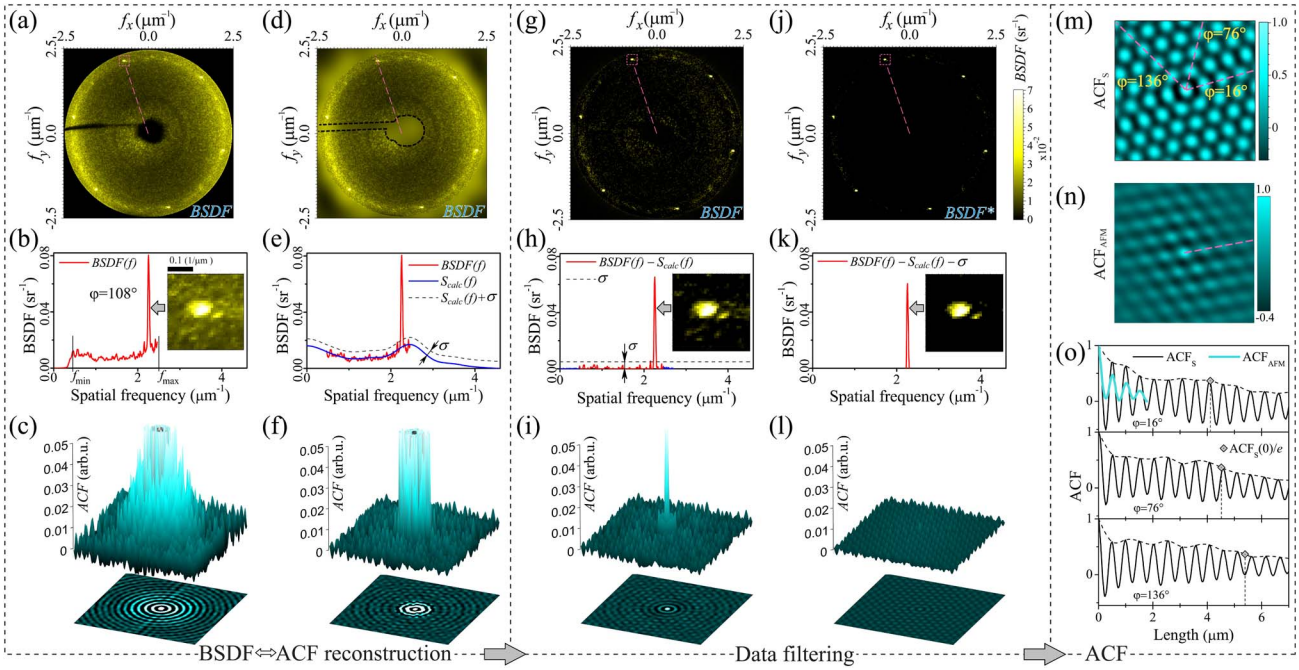

Fig. 2. (a) BSDF as measured by ARHELS versus spatial frequencies f_x and f_y for x and y Cartesian coordinate directions of the surface. (d) $S(f)$: BSDF with low-resolution approximation $S_{\mathrm{calc}}(f)$. (g) Filtered BSDF with residual noise level σ. (j) Filtered BSDF without residual noise level σ. Dashed lines in BSDF indicatrices identify cross-sections shown in (b), (e), (h), (k). Insets in (b), (h), (k) show the structure of the single diffraction peak in BSDF indicatrix. (c), (f), (i), (l): the 4×4 μm^2 ACF images computed by applying inverse Fourier transform to BSDF data shown in (a), (d), (g), (j), correspondingly. (m) Normalized 3.7×3.7 μm^2 image of ACF shown in (l), as obtained after filtering of BSDF data. (n) 3.7×3.7 μm^2 ACF image obtained by AFM. (o) Cross-sections of ACF images along dashed lines shown in (m) and (n). Filled diamond identifies the value $\mathrm{ACF} = \mathrm{ACF}_s(0)/e$ at the autocorrelation length.

random phase. The trial function of the surface height $h'_n(r)$ in the nth iteration is obtained by the inverse Fourier transform of $G_n(f)$. Since the surface profile $h(r)$ has to be a real function that can acquire negative values [1], this constraint is applied to obtain the next $n+1$ iteration $h_{n+1}(r)$. γ_h in Fig. 1(b) is the area where the $h(r)$ is nonzero for the ER procedure [11]. The phase of the roughness spectrum was reconstructed via Fourier transform of $h_{n+1}(r)$. The obtained distribution $G_{\text{calc}}(f)$ and its phase function φ are used for successive reconstruction of the roughness spectrum $G_{n+1}(f)$.

One of the major obstacles in the reconstruction of the surface profile at the mesoscale is the presence of a substantial scattering background, including diffuse scattering caused by random surface relief. Therefore, this background has to be filtered out from the light diffraction pattern. A presence of diffuse scattering for the photonic crystal PC1 introduces significant errors in the calculation of PSD. Nevertheless, in terms of a "scatter prediction" approach [1] the BSDF can be considered as a function that describes surface statistics sufficiently close to the real PSD. Therefore, the BSDF was used instead of PSD in retrieval algorithms for the sample PC1.

The BSDF indicatrix and its cross-section obtained with laser light wavelength $\lambda = 405$ nm for sample PC1 are shown in Figs. 2(a) and 2(b). Measured BSDF data are available only within a short range of spatial frequencies: $f_{\text{obs}} = \sin\theta/\lambda$, from $f_{\min} = 0.45\ \mu\text{m}^{-1}$ to $f_{\max} = \sin 90°/\lambda = 2.47\ \mu\text{m}^{-1}$. The area of the indicatrix for $f < f_{\min}$ is blocked by the sample holder. The absence of experimental data for $f < f_{\min}$ and $f > f_{\max}$ introduces significant error into the calculation of ACF from BSDF [Fig. 2(c)]. This issue can be removed by iterative reconstruction of BSDF where experimental data are absent by using ER or HIO algorithms, as shown in Fig. 1(b). Applying low-resolution approximation, the retrieval procedure reconstructs only the smooth component $S_{\text{calc}}(f)$ of BSDF(f) caused by random surface irregularities, excluding sharp diffraction peaks from the object [Figs. 2(d) and 2(e)]. The low-resolution function $S_{\text{calc}}(f)$ was obtained by choosing the sufficiently small area γ_{ACF}.

The scattering component caused by random irregularities can be filtered out by subtracting the function $S_{\text{calc}}(f)$ from the BSDF indicatrix, as shown in Figs. 2(g) and 2(h). This step greatly improves the ACF [Fig. 2(i)]. The final filtering includes subtracting from BSDF a residual noise level σ [Figs. 2(j) and 2(k)]. It is important, however, to avoid possible filtering of informative diffraction peaks and their satellites, which are critical for correct reconstruction of the ACF [Fig. 2(l)].

The autocorrelation function ACF_s retrieved from the filtered BSDF [Fig. 2(m)] shows striking similarity with ACF_{AFM} obtained directly by atomic force microscopy (AFM) [Fig. 2(n)]. ACF_s and ACF_{AFM} images show the same pattern and same period of oscillations along equivalent cross-sections [Fig. 2(o)].

The last computational step in Fig. 1(b) provides the reconstruction of the surface profile h. Here it is important to choose correctly the size of the area γ_h. The shape of γ_h is a circle with diameter equal to or smaller than the diameter of the laser beam. The algorithm convergence with reproducible profile h was obtained when the diameter d of γ_h had been set equal to the averaged value of autocorrelation length $\xi = 5$ μm.

The reconstruction of $h(r)$ starts with the input function $G_0(f) = \sqrt{S^*(f)} \times e^{i\varphi_{rnd}}$ [see Fig. 1(b)], where $S^*(f)$ is the filtered BSDF shown in Fig. 2(j). To avoid a stagnation of the phase-retrieval algorithm and to improve its convergence, the initial shape of the area γ_h was chosen as a semicircle with diameter $d = \xi/2$ [12]. After applying consecutively six ER and two HIO iterations in 30 cycles, the area γ_h was set to its final circular shape with $d = \xi$. By a combination of six ER and three HIO iterations in 100 cycles we obtained a robust reproducible reconstruction of the phase φ and surface profile h with all peculiarities.

The surface topography h_{AFM} obtained by AFM [Fig. 3(a)] shows close resemblance with the topography h reconstructed from scattering data [Fig. 3(b)]. Since the reconstruction of h was performed by using BSDF data instead of the exact PSD, only an arbitrary amplitude of h is obtained. Nevertheless, the cross-sections of the h_{AFM} and h images show remarkable quantitative coincidence of surface profiles for lateral direction [Fig. 3(c)].

The proposed diffractive imaging technique can be also applied for quantitative reconstruction of surface heights if the average height of irregularities is much less than the wavelength of illumination and diffuse scattering is negligible. For this study we used the plasmonic crystal PC2 formed by gold nanopyramids [Figs. 4(a) and 4(b)]. The PSD function was calculated using Elson's theory [13] applied to ARHELS data obtained with a He–Ne laser ($\lambda = 632.8$ nm). Figure 4(c) shows the filtered power spectral density function PSD* without background caused by random scatterers. By using input function $S^* = \text{PSD}^*$ in the phase-retrieval algorithm [see Fig. 1(b)], we obtained the surface topography h shown in Fig. 4(f).

The quality of reconstructed topography h can be significantly improved by applying some predictions for PSD distribution, achieving super-resolution. Thus, for a periodical object such as this plasmonic crystal, the filtered PSD* can be roughly approximated by a sum of a sinusoidal surface component PSD_{sin} and component PSD_Δ caused by random deviation of the surface topography from its sinusoidal shape, as follows:

$$\text{PSD}^* \approx \text{PSD}_{\text{sin}} + \text{PSD}_\Delta. \quad (1)$$

According to the theory of optical diffraction, the smooth sinusoidal surface contributes to higher orders of light

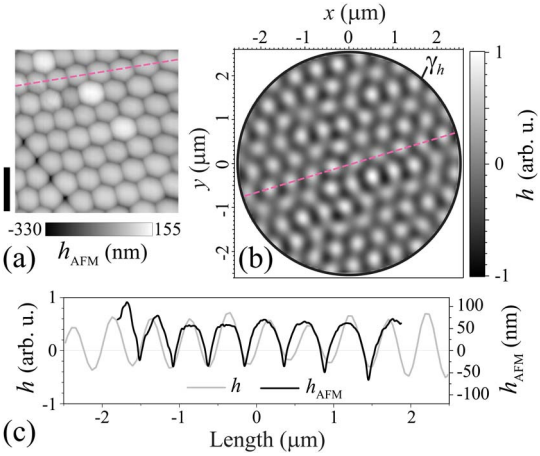

Fig. 3. (a) AFM image of photonic crystal PC1. The scale bar indicates 1 μm. (b) The surface topography h reconstructed from ARHELS data. (c) Cross-sections of AFM and h images along dashed lines shown in (a) and (b).

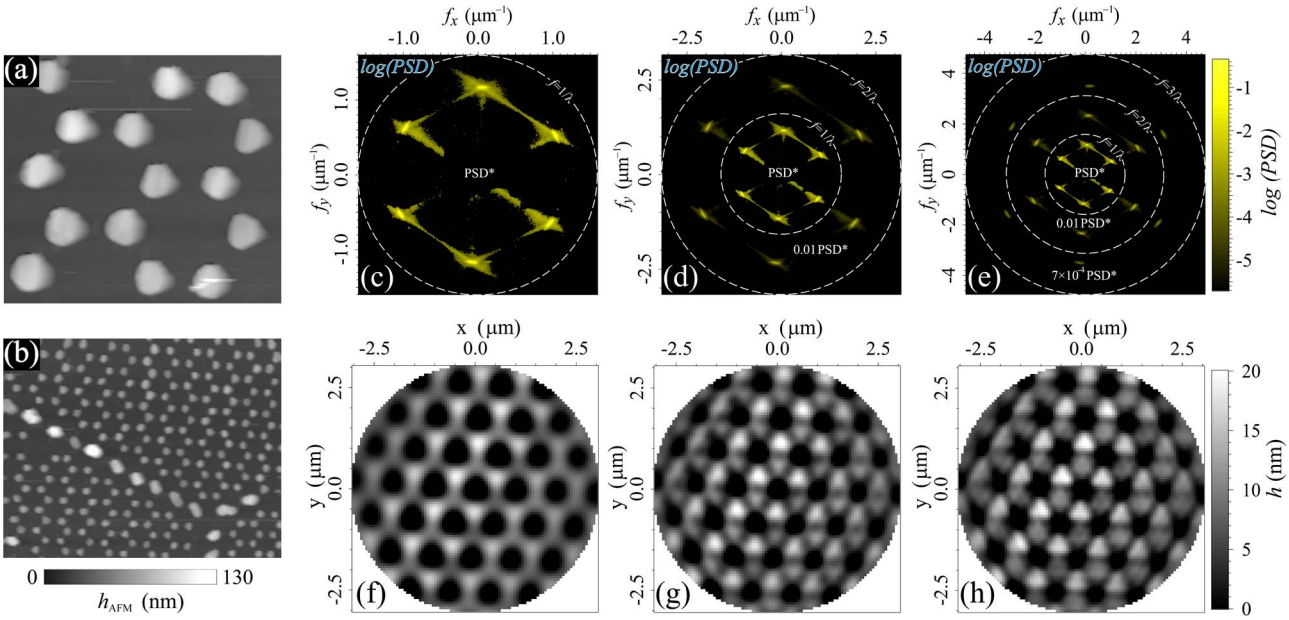

Fig. 4. AFM images of plasmonic crystal PC2: (a) 2.7×2.4 μm^2 scan, (b) 12.3×9.6 μm^2 scan. (c) Filtered PSD* as obtained from ARHELS data. (d) PSD* with reconstructed part at $f_{max} < f < 2f_{max}$ and (e) at $2f_{max} < f < 3f_{max}$. The correspondingly reconstructed surface topographies h are shown in (f), (g), (h).

diffraction much less than the random roughness. Therefore, we consider here only the contribution of PSD_Δ into higher harmonics at $f > f_{max}$. Assuming a fractal-like distribution of random scatterers, the PSD_Δ follows an inverse power law, which can be written as $PSD_\Delta = \tilde{K}_n/f^{n+1}$ [14], where $\tilde{K}_n$ and n are fractal parameters.

In our model we assume that the power spectrum contains ~25% of a random component as $PSD_\Delta(f < f_{max}) = 0.25PSD^*$ and that it reduces to 1% within $f_{max} < f < 2f_{max}$ as $PSD_\Delta = 0.01PSD^*$ [Fig. 4(d)]. In this tentative model the fractal parameter $n = 2.83$ corresponds to a marginal fractal of smooth surface [14,15], a good estimation for the sample studied. Using this parameter, the power spectrum within $2f_{max} < f < 3f_{max}$ was found as $PSD_\Delta = 7 \times 10^{-4}PSD^*$ [Fig. 4(e)].

The reconstructed surface topography h from extrapolated PSD* into $f_{max} < f < 2f_{max}$ and $2f_{max} < f < 3f_{max}$ regions is shown in Figs. 4(g) and 4(h), respectively. Achieved super-resolution in topography function h of the sample PC2 shows fairly close proximity to the topography h_{AFM} obtained by AFM [Figs. 4(a) and 4(b)]. Discrepancies between h and h_{AFM} are related to the lack of measured scattering data for spatial frequencies that are beyond the available scattering bandwidth.

In summary, it has been experimentally demonstrated that the reconstruction of surface shape can be obtained for submicron structures even in the presence of diffuse scattering by applying diffractive imaging retrieval algorithms. Subsequent calculation of ACF provides additional reconstruction of PSD function and its filtering to perform final reconstruction of surface topography. The proposed procedure to filter the scattering background can be applied for any type of periodical as well as nonperiodical object. We demonstrated the experimental technique that enables not only quantitative reconstruction of the surface profile but also super-resolution. These results open new prospects for subwavelength diffractive imaging in light scattering metrology.

Funding. National Science Foundation (NSF) (DMR-1531627); Army Research Office (ARO) (W911NF-15-1-0448).

REFERENCES

1. J. C. Stover, *Optical Scattering: Measurements and Analysis* (SPIE Optical Engineering, 1995).
2. W. Osten, W. Faridian, P. Gao, K. Körner, D. Naik, G. Pedrini, A. Singh, M. Takeda, and M. Wilke, Appl. Opt. **53**, G44 (2014).
3. Y. Jo, J. Jung, J. W. Lee, D. Shin, H. Park, K. T. Nam, J.-H. Park, and Y. Park, Sci. Rep. **4**, 5090 (2014).
4. J. Bertolotti, E. van Putten, B. Christian, A. Lagendijk, W. Vos, and A. Mosk, Nature **491**, 232 (2012).
5. R. W. Gerchberg and W. O. Saxton, Optik **35**, 237 (1972).
6. J. R. Fienup, Appl. Opt. **21**, 2758 (1982).
7. N. Denkov, O. Velev, P. Kralchevski, I. Ivanov, H. Yoshimura, and K. Nagayama, Langmuir **8**, 3183 (1992).
8. M. R. Gonçalves, A. Siegel, and O. Marti, J. Microsc. **229**, 475 (2008).
9. V. Sterligov and P. Cheyssac, "Appareil et procédé de caractérisation optique d'un objet," French patent 0115232 (November 23, 2001).
10. V. A. Sterligov, P. Cheyssac, G. Bossis, and C. Metayer, in *Conference on Lasers and Electro-Optics*, OSA Technical Digest (2004), paper CThII2.
11. J. R. Fienup, T. Crimmins, and W. Holsztynski, J. Opt. Soc. Am. **72**, 610 (1982).
12. J. Fienup and C. Wackerman, J. Opt. Soc. Am. A **3**, 1897 (1986).
13. J. M. Elson, Phys. Rev. B **12**, 2541 (1975).
14. E. L. Church, Appl. Opt. **27**, 1518 (1988).
15. M. V. Berry, J. Phys. A **12**, 781 (1979).